

See discussions, stats, and author profiles for this publication at: <https://www.researchgate.net/publication/228093049>

Photoluminescent Lanthanide–Organic 2D Networks: A Combined Synchrotron Powder X-ray Diffraction and Solid-State NMR Study

ARTICLE *in* CHEMISTRY OF MATERIALS · JUNE 2007

Impact Factor: 8.35 · DOI: 10.1021/cm070596q

CITATIONS

46

READS

22

6 AUTHORS, INCLUDING:



Luís Cunha Silva

University of Porto

111 PUBLICATIONS 1,080 CITATIONS

SEE PROFILE



Luís Mafra

University of Aveiro

87 PUBLICATIONS 1,257 CITATIONS

SEE PROFILE



Luís D Carlos

University of Aveiro

483 PUBLICATIONS 9,770 CITATIONS

SEE PROFILE



Joao Rocha

University of Aveiro

455 PUBLICATIONS 9,826 CITATIONS

SEE PROFILE

Photoluminescent Lanthanide–Organic 2D Networks: A Combined Synchrotron Powder X-ray Diffraction and Solid-State NMR Study

Luís Cunha-Silva,[†] Luís Mafra,[†] Duarte Ananias,[†] Luís D. Carlos,[‡] João Rocha,[†] and Filipe A. Almeida Paz^{*,†}

Departments of Chemistry and Physics, University of Aveiro, CICECO, 3810-193 Aveiro, Portugal

Received March 2, 2007. Revised Manuscript Received April 19, 2007

A series of two-dimensional lanthanide–organic materials (LnOFs), [Ln(H₃NMP)]·1.5H₂O [Ln³⁺ = La³⁺ (1), Pr³⁺ (2), Nd³⁺ (3), Sm³⁺ (4), or Eu³⁺ (5); H₃NMP^{3−} is a residue of nitrilotris(methylenephosphonic acid)], has been isolated as microcrystalline powders from hydrothermal synthesis and characterized by high-resolution laboratory and synchrotron powder X-ray diffraction (PXRD), solid-state NMR, FTIR and FT Raman spectroscopies, CHN elemental analysis, thermogravimetry, scanning electron microscopy, and energy dispersive analysis of X-ray spectroscopy. The crystal structure of [Pr(H₃NMP)]·1.5H₂O (2) has been solved from a combined study of ab initio methods using high-resolution PXRD data and high-resolution solid-state NMR techniques performed on [La(H₃NMP)]·1.5H₂O (1) (¹³C, ¹⁵N, ³¹P CPMAS and 2D ¹H–¹H/³¹P HOMCOR/HETCOR). The structure contains a single lanthanide center which does not have water molecules in its first coordination sphere. This Ln³⁺ center acts as the node of a neutral undulated two-dimensional network, ∞²[Pr(H₃NMP)], having a (4,4) topology, which close packs along the [100] direction of the unit cell (adjacent layers are related by inversion). Water molecules of crystallization occupy the interlayer spaces, and a one-dimensional water cluster (spiral chain topology) is confined to the channels formed by the packing of adjacent layers. Removal of these water molecules (investigated by variable-temperature PXRD) leads to a new crystalline phase with a smaller interlayer space. The material partially reabsorbs water from the surrounding environment, originating the parent phase. This dehydration/rehydration process has also been monitored by photoluminescence (PL) spectroscopy, revealing that the presence of water in the interlayer spaces does not affect much the PL properties of [Eu(H₃NMP)]·1.5H₂O (5).

1. Introduction

The design and synthesis of coordination-based functional multidimensional (i.e., 1D, 2D, and 3D) materials has been a very active field of research in recent years. The remarkable growth in interest surrounding these compounds, commonly designated as coordination polymers, metal–organic frameworks (MOFs), or even (more recently) as coordination frameworks, is largely motivated by the discovery of new and intriguing structural architectures exhibiting exciting properties with potential use in a wide range of industrial applications.¹ Both carboxylic acid groups² and phosphonic acid based ligands have been much investigated as primary building blocks, and recent reviews are available in the literature.^{3,4}

Most structural studies on metal phosphonate-type MOFs have been focused on first-row transition metals (d-block elements) and main-group metals such as Al³⁺, Ga³⁺, and Pb²⁺. These elements have been preferred over, for example, the lanthanides (f-block elements) because the latter usually have larger coordination numbers with variable coordination geometries. These lanthanide features lead to supramolecular isomerism⁵ and a high probability of occurrence of bonding

“mistakes” which, allied with the well-known low solubility in water and many organic solvents, usually results in isolation of microcrystalline powders instead of single crystals.⁶ Nevertheless, lanthanides such as Eu³⁺, Sm³⁺, and Tb³⁺ are of great interest because they allow the crystal engineering of materials with photoluminescence properties.⁵ To improve the solubility and crystallinity of lanthanide phosphonates some additional functional groups such as

- (1) Kepert, C. J. *Chem. Commun.* **2006**, 695–700. Li, H.; Eddaoudi, M.; O’Keeffe, M.; Yaghi, O. M. *Nature* **1999**, *402*, 276–279. Chen, B. L.; Eddaoudi, M.; Hyde, S. T.; O’Keeffe, M.; Yaghi, O. M. *Science* **2001**, *291*, 1021–1023. Eddaoudi, M.; Kim, J.; Rosi, N.; Vodak, D.; Wachter, J.; O’Keeffe, M.; Yaghi, O. M. *Science* **2002**, *295*, 469–472. Rosi, N. L.; Eckert, J.; Eddaoudi, M.; Vodak, D. T.; Kim, J.; O’Keeffe, M.; Yaghi, O. M. *Science* **2003**, *300*, 1127–1129. Yaghi, O. M.; O’Keeffe, M.; Ockwig, N. W.; Chae, H. K.; Eddaoudi, M.; Kim, J. *Nature* **2003**, *423*, 705–714. Chae, H. K.; Siberio-Perez, D. Y.; Kim, J.; Go, Y.; Eddaoudi, M.; Matzger, A. J.; O’Keeffe, M.; Yaghi, O. M. *Nature* **2004**, *427*, 523–527. Kitagawa, S.; Uemura, K. *Chem. Soc. Rev.* **2005**, *34*, 109–119; Rowsell, J. L. C.; Spencer, E. C.; Eckert, J.; Howard, J. A. K.; Yaghi, O. M. *Science* **2005**, *309*, 1350–1354.
- (2) Guillou, O.; Daiguebonne, C. Lanthanide-containing Coordination Polymers. In *Handbook on the Physics and Chemistry of Rare Earths*; Gschneidner, K. A., Bunzli, J.-C. G., Pecharsky, V. K., Eds.; Elsevier B. V.: New York, 2005; Vol. 34, pp 359–404. Ye, B. H.; Tong, M. L.; Chen, X. M. *Coord. Chem. Rev.* **2005**, *249*, 545–565. Rowsell, J. L. C.; Yaghi, O. M. *Microporous Mesoporous Mater.* **2004**, *73*, 3–14. Kesanli, B.; Lin, W. B. *Coord. Chem. Rev.* **2003**, *246*, 305–326.

* To whom correspondence should be addressed. Phone: (+351) 234 370200. Fax: (+351) 234 370084. E-mail: fpaz@dq.ua.pt.

[†] Department of Chemistry.

[‡] Department of Physics.

calixarenes, crown ethers, hydroxyl, carboxylates, sulfonates, and amines have been combined with the phosphonate ligands.^{4,7–9} Hence, research on lanthanide–organic frameworks (LnOFs) involving phosphonate ligands has been focused essentially on monophosphonic and diphosphonic acids and their derivatives. To the best of our knowledge, the number of LnOFs involving highly flexible polyphosphonic acid ligands (i.e., two or more phosphonate groups) is scarce.

Following our interest in crystalline MOFs¹⁰ we recently focused our attention on *N*-(phosphonomethyl)iminodiacetic acid (H₄pmida), a versatile chelating organic ligand displaying two carboxylate groups and a single phosphonate group.¹¹ At present we are exploring the use of polyphosphonic acid ligands, such as nitrilotris(methylphosphonic acid) (H₆NMP) to prepare novel LnOFs. This molecule has been largely disregarded in the preparation of crystalline functional materials.^{12,13}

Here, we report a novel series of 2D LnOFs obtained from the hydrothermal reaction between H₆NMP and lanthanide ions, [Ln(H₃NMP)]·1.5H₂O [Ln³⁺ = La³⁺ (**1**), Pr³⁺ (**2**), Nd³⁺ (**3**), Sm³⁺ (**4**), and Eu³⁺ (**5**)]. All compounds were isolated as microcrystalline powders, which made a full structure

elucidation by single-crystal X-ray diffraction impossible. Even though PXRD studies are well disseminated for inorganic materials and, more recently, organic compounds of pharmaceutical importance have also been the subject of several investigations. However, the determination of MOFs structures from powder data is far less common due to the inherent difficulties associated with the extraction of intensities.¹⁴ For the [Ln(H₃NMP)]·1.5H₂O series we used in tandem high-resolution PXRD and high-resolution solid-state NMR techniques in order to unveil the structural details of these materials. This latter technique is a powerful tool to probe selectively the local environment of distinct nuclei. In particular, it provided a solid approach to the location of ¹H nuclei,¹⁵ which was of crucial importance during the structural refinement of Ln(H₃NMP)]·1.5H₂O.

2. Experimental Section

2.1. Synthesis of [Ln(H₃NMP)]·1.5H₂O. A suspension containing the respective lanthanide chloride (LnCl₃·*n*H₂O, Ln³⁺ = La³⁺, Pr³⁺, Nd³⁺, Sm³⁺, and Eu³⁺) and nitrilotris(methylenephosphonic acid) [H₆NMP, N(CH₂PO₃H₂)₃; 97%, Fluka] in distilled water (molar ratios 1:1:650, respectively) was stirred thoroughly for 90 min at ambient temperature. The resulting homogeneous suspension was transferred to a Teflon-lined Parr Instruments autoclave and placed inside a MMM Venticell oven (Confort model with minicomputer-controlled temperature program) to react at 438 K for 2 days (26 days for material **3**). Each reaction vessel was then allowed to cool slowly to ambient temperature (while inside the oven) before opening. Microcrystalline powders of [Ln(H₃NMP)]·1.5H₂O [Ln³⁺ = La³⁺ (**1**), Pr³⁺ (**2**), Nd³⁺ (**3**), Sm³⁺ (**4**), and Eu³⁺ (**5**)] were recovered by vacuum filtration, washed with copious amounts of distilled water, and air-dried.

Anal. calcd (%) for C₃H₁₂NO_{10.5}P₃La (**1**): C, 7.80; H, 2.62; N, 3.03 (C/N = 2.57). Found: C, 7.30; H, 2.51; N, 2.85 (C/N = 2.56). Anal. calcd (%) for C₃H₁₂NO_{10.5}P₃Pr (**2**): C, 7.77; H, 2.60; N, 3.02 (C/N = 2.57). Found: C, 6.61; H, 2.39; N, 2.58 (C/N = 2.56).

- (3) Matczak-Jon, E.; Videnova-Adrabinska, V. *Coord. Chem. Rev.* **2005**, *249*, 2458–2488. Mutin, P. H.; Guerrero, G.; Vioux, A. *J. Mater. Chem.* **2005**, *15*, 3761–3768. Maeda, K. *Microporous Mesoporous Mater.* **2004**, *73*, 47–55. Demadis, K. D.; Katarachia, S. D. *Phosphorus Sulfur* **2004**, *179*, 627–648. Vioux, A.; Le Bideau, J.; Mutin, P. H.; Leclercq, D. Hybrid organic-inorganic materials based on organophosphorus derivatives. In *New Aspects in Phosphorus Chemistry IV*; 2004; Vol. 232; pp 145–174. Clearfield, A. *Curr. Opin. Solid State Mater.* **2002**, *6*, 495–506.
- (4) Clearfield, A.; Sharma, C. V. K.; Zhang, B. P. *Chem. Mater.* **2001**, *13*, 3099–3112.
- (5) Bunzli, J. C. G. *Acc. Chem. Res.* **2006**, *39*, 53–61. Bunzli, J. C. G.; Piguet, C. *Chem. Soc. Rev.* **2005**, *34*, 1048–1077.
- (6) Champness, N. R. Making Coordination Frameworks. In *Making Crystals by Design-Methods, Techniques and Applications*, 1st ed.; Braga, D., Grepioni, F., Eds.; Wiley-VCH Verlag GmbH & Co. KGaA: Weinheim, 2007; pp 193–208.
- (7) Ngo, H. L.; Lin, W. B. *J. Am. Chem. Soc.* **2002**, *124*, 14298–14299. Plutnar, J.; Rohovec, J.; Kotek, J.; Zak, Z.; Lukes, I. *Inorg. Chim. Acta* **2002**, *335*, 27–35. Evans, O. R.; Ngo, H. L.; Lin, W. B. *J. Am. Chem. Soc.* **2001**, *123*, 10395–10396. Bligh, S. W. A.; Choi, N.; Geraldes, C.; Knoke, S.; McPartlin, M.; Sangane, M. J.; Woodroffe, T. M. *Dalton Trans.* **1997**, 4119–4125.
- (8) Tang, S.-F.; Song, J. L.; Mao, J. G. *Eur. J. Inorg. Chem.* **2006**, *2006*, 2011–2019. Du, Z. Y.; Xu, H. B.; Mao, J. G. *Inorg. Chem.* **2006**, *45*, 9780–9788. Tang, S. F.; Song, J. L.; Li, X. L.; Mao, J. G. *Cryst. Growth Des.* **2006**, *6*, 2322–2326. Gan, X. M.; Binyamin, I.; Pailloux, S.; Duesler, E. N.; Paine, R. T. *Dalton Trans.* **2006**, 3912–3917. Vojtisek, P.; Cigler, P.; Kotek, J.; Rudovsky, J.; Hermann, P.; Lukes, I. *Inorg. Chem.* **2005**, *44*, 5591–5599. Song, J. L.; Lei, C.; Mao, J. G. *Inorg. Chem.* **2004**, *43*, 5630–5634. Tei, L.; Blake, A. J.; Wilson, C.; Schroder, M. *Dalton Trans.* **2004**, 1945–1952. Van Meervelt, L.; Martello, P.; Silvestre, J. P.; Rochdaoui, R.; Lee, M. R.; Dao, N. Q.; Gorller-Walrand, C. Z. *Kristallogr.* **2002**, *217*, 27–34. Serpaggi, F.; Ferey, G. *J. Mater. Chem.* **1998**, *8*, 2737–2741.
- (9) Song, J. L.; Mao, J. G. *Chem.—Eur. J.* **2005**, *11*, 1417–1424.
- (10) Soares-Santos, P. C. R.; Paz, F. A. A.; Ferreira, R. A. S.; Klinowski, J.; Carlos, L. D.; Trindade, T.; Nogueira, H. I. S. *Polyhedron* **2006**, *25*, 2471–2482. Klinowski, J.; Paz, F. A.; Bell, R. *Chem. Ind.* **2005**, 24–27. Paz, F. A. A.; Bond, A. D.; Khimiyak, Y. Z.; Klinowski, J. *Acta Crystallogr., Sect. C* **2002**, *58*, M608–M610. Paz, F. A. A.; Bond, A. D.; Khimiyak, Y. Z.; Klinowski, J. *Acta Crystallogr., Sect. E* **2002**, *58*, M691–M693. Paz, F. A. A.; Khimiyak, Y. Z.; Bond, A. D.; Rocha, J.; Klinowski, J. *Eur. J. Inorg. Chem.* **2002**, 2823–2828. Paz, F. A. A.; Klinowski, J. *J. Phys. Org. Chem.* **2003**, *16*, 772–782. Paz, F. A. A.; Klinowski, J. *Chem. Commun.* **2003**, 1484–1485. Paz, F. A. A.; Klinowski, J. *J. Solid State Chem.* **2004**, *177*, 3423–3432. Paz, F. A. A.; Klinowski, J. *Inorg. Chem.* **2004**, *43*, 3882–3893. Paz, F. A. A.; Klinowski, J. *Inorg. Chem.* **2004**, *43*, 3948–3954.
- (11) Shi, F. N.; Paz, F. A. A.; Girginova, P. I.; Amaral, V. S.; Rocha, J.; Klinowski, J.; Trindade, T. *Inorg. Chim. Acta* **2006**, *359*, 1147–1158. Shi, F. N.; Paz, F. A. A.; Trindade, T.; Rocha, J. *Acta Crystallogr., Sect. E* **2006**, *62*, M335–M338. Paz, F. A. A.; Shi, F. N.; Trindade, T.; Klinowski, J.; Rocha, J. *Acta Crystallogr., Sect. E* **2005**, *61*, M2247–M2250. Mafra, L.; Paz, F. A. A.; Shi, F. N.; Rocha, J.; Trindade, T.; Fernandez, C.; Makal, A.; Wozniak, K.; Klinowski, J. *Chem.—Eur. J.* **2005**, *12*, 363–375. Paz, F. A. A.; Rocha, J.; Klinowski, J.; Trindade, T.; Shi, F. N.; Mafra, L. *Prog. Solid State Chem.* **2005**, *33*, 113–125. Paz, F. A. A.; Shi, F. N.; Klinowski, J.; Rocha, J.; Trindade, T. *Eur. J. Inorg. Chem.* **2004**, 2759–2768. Shi, F. N.; Paz, F. A. A.; Girginova, P.; Rocha, J.; Amaral, V. S.; Klinowski, J.; Trindade, T. *J. Mol. Struct.* **2006**, *789*, 200–208. Shi, F. N.; Paz, F. A. A.; Girginova, P. I.; Mafra, L.; Amaral, V. S.; Rocha, J.; Makal, A.; Wozniak, K.; Klinowski, J.; Trindade, T. *J. Mol. Struct.* **2005**, *754*, 51–60.
- (12) Demadis, K. D.; Katarachia, S. D.; Raptis, R. G.; Zhao, H.; Baran, P. *Cryst. Growth Des.* **2006**, *6*, 836–838. Cabeza, A.; Aranda, M. A. G.; Bruque, S.; J. *Mater. Chem.* **1999**, *9*, 571–578. Cabeza, A.; Bruque, S.; Guagliardi, A.; Aranda, M. A. G. *J. Solid State Chem.* **2001**, *160*, 278–286. Cabeza, A.; Xiang, O. Y.; Sharma, C. V. K.; Aranda, M. A. G.; Bruque, S.; Clearfield, A. *Inorg. Chem.* **2002**, *41*, 2325–2333.
- (13) Bakhmutova-Albert, E. V.; Bestaoui, N.; Bakhmutov, V. I.; Clearfield, A.; Rodriguez, A. V.; Llavona, R. *Inorg. Chem.* **2004**, *43*, 1264–1272.
- (14) Espallargas, G. M.; Brammer, L. Diffraction Studies in Crystal Engineering. In *Making Crystals by Design-Methods, Techniques and Applications*, 1st ed.; Braga, D., Grepioni, F., Eds.; Wiley-VCH Verlag GmbH & Co. KGaA: Weinheim, 2007; pp 241–265.
- (15) Dutour, J.; Guillou, N.; Huguenard, C.; Taulelle, F.; Mellot-Draznieks, C.; Ferey, G. *Solid State Sci.* **2004**, *6*, 1059–1067. Harris, R. K. *Solid State Sci.* **2004**, *6*, 1025–1037.

Anal. calcd (%) for $\text{C}_3\text{H}_{12}\text{NO}_{10.5}\text{P}_3\text{Nd}$ (**3**): C, 7.70; H, 2.59; N, 3.00 (C/N = 2.57). Found: C, 7.16; H, 2.41; N, 2.79 (C/N = 2.57). Anal. calcd (%) for $\text{C}_3\text{H}_{12}\text{NO}_{10.5}\text{P}_3\text{Sm}$ (**4**): C, 7.61; H, 2.55; N, 2.96 (C/N = 2.57). Found: C, 6.68; H, 2.38; N, 2.66 (C/N = 2.51). Anal. calcd (%) for $\text{C}_3\text{H}_{12}\text{NO}_{10.5}\text{P}_3\text{Eu}$ (**5**): C, 7.59; H, 2.55; N, 2.95 (C/N = 2.57). Found: C, 6.77; H, 2.30; N, 2.72 (C/N = 2.49).

Selected ATR-FTIR data (FT Raman data in *italics* inside the parentheses) (cm^{-1}). **1**: $\nu(\text{O}-\text{H}, \text{water}) = 3348 \text{ w}$, $\nu_{\text{sym}}(\text{N}-\text{H}) = 3111 \text{ m}$ (3114 w), $\nu(\text{C}-\text{H}$ and $\text{P}-\text{OH}) = 3050-2900 \text{ w}$ (3029 w, 3009 w, 2981 m, 2961 vs, 2939 s), $\delta(\text{P}-\text{OH}) = 2326 \text{ w}$, $\nu_{\text{sym}}(\text{P}=\text{O}) = 1186, 1164 \text{ vs}$ (1162 vs), $\nu_{\text{asym}}(\text{P}-\text{O}_{\text{coord}}) = 1069 \text{ vs}$ (1080 vs), $\nu_{\text{sym}}(\text{P}-\text{O}_{\text{coord}}) = 1024, 997 \text{ vs}$ (1010 s, 998 m), and $\nu_{\text{sym}}(\text{P}-\text{OH}) = 907 \text{ vs}$ (911 m). **2**: $\nu(\text{O}-\text{H}, \text{water}) = 3355 \text{ w}$, $\nu_{\text{sym}}(\text{N}-\text{H}) = 3110 \text{ m}$ (3114 w), $\nu(\text{C}-\text{H}$ and $\text{P}-\text{OH}) = 3050-2900 \text{ w}$ (3033 w, 3007 w, 2981 m, 2964 vs, 2939 s), $\delta(\text{P}-\text{OH}) = 2360, 2322 \text{ w}$, $\nu_{\text{sym}}(\text{P}=\text{O}) = 1185, 1164 \text{ vs}$ (1162 vs), $\nu_{\text{asym}}(\text{P}-\text{O}_{\text{coord}}) = 1066 \text{ vs}$ (1079 vs), $\nu_{\text{sym}}(\text{P}-\text{O}_{\text{coord}}) = 1021, 998 \text{ vs}$ (1011 vs), and $\nu_{\text{sym}}(\text{P}-\text{OH}) = 912 \text{ vs}$ (917 vs). **3**: $\nu(\text{O}-\text{H}, \text{water}) = 3352 \text{ w}$, $\nu_{\text{sym}}(\text{N}-\text{H}) = 3109 \text{ m}$ (3114 w), $\nu(\text{C}-\text{H}$ and $\text{P}-\text{OH}) = 3050-2900 \text{ w}$ (3035 w, 3008 w, 2981 m, 2965 vs, 2939 s), $\delta(\text{P}-\text{OH}) = 2360, 2333 \text{ w}$, $\nu_{\text{sym}}(\text{P}=\text{O}) = 1184, 1165 \text{ vs}$ (1165 vs), $\nu_{\text{asym}}(\text{P}-\text{O}_{\text{coord}}) = 1065 \text{ vs}$ (1078 vs), $\nu_{\text{sym}}(\text{P}-\text{O}_{\text{coord}}) = 1020, 997 \text{ vs}$ (1012 vs), and $\nu_{\text{sym}}(\text{P}-\text{OH}) = 911 \text{ vs}$ (918 s). **4**: $\nu(\text{O}-\text{H}, \text{water}) = 3352 \text{ w}$ (3398 w, 3329 w), $\nu_{\text{sym}}(\text{N}-\text{H}) = 3109 \text{ m}$ (3120 w), $\nu(\text{C}-\text{H}$ and $\text{P}-\text{OH}) = 3050-2900 \text{ w}$ (2991 s, 2960 vs, 2933 s), $\delta(\text{P}-\text{OH}) = 2360, 2322 \text{ w}$, $\nu_{\text{sym}}(\text{P}=\text{O}) = 1186 \text{ vs}$ (1170 vs), $\nu_{\text{asym}}(\text{P}-\text{O}_{\text{coord}}) = 1063 \text{ vs}$ (1070 vs), $\nu_{\text{sym}}(\text{P}-\text{O}_{\text{coord}}) = 1021, 998 \text{ vs}$ (1034 vs, 1010 vs), and $\nu_{\text{sym}}(\text{P}-\text{OH}) = 913 \text{ vs}$ (918 vs). **5**: $\nu(\text{O}-\text{H}, \text{water}) = 3340 \text{ w}$, $\nu_{\text{sym}}(\text{N}-\text{H}) = 3109 \text{ m}$ (3113 w), $\nu(\text{C}-\text{H}$ and $\text{P}-\text{OH}) = 3050-2900 \text{ w}$ (3039 w, 3015 w, 2970 vs, 2939 vs), $\delta(\text{P}-\text{OH}) = 2360 \text{ m}$, $\nu_{\text{sym}}(\text{P}=\text{O}) = 1186 \text{ vs}$ (1173 vs), $\nu_{\text{asym}}(\text{P}-\text{O}_{\text{coord}}) = 1064 \text{ vs}$ (1077 vs), $\nu_{\text{sym}}(\text{P}-\text{O}_{\text{coord}}) = 1020 \text{ m}$, 999 vs (1016 vs, 1005 s), and $\nu_{\text{sym}}(\text{P}-\text{OH}) = 914 \text{ vs}$ (924 vs).

Thermogravimetric analysis (TGA) data (weight losses in %) and derivative thermogravimetric peaks (DTG; in *italics* inside the parentheses). **1**: 20–60 °C –0.7% (43 °C), 60–130 °C –4.1% (100 °C), 130–320 °C –1.2%, 320–405 °C –2.0% (367 °C), and 405–675 °C –5.8% (446 °C). **2**: 23–70 °C –1.7% (32 °C), 70–120 °C –3.6% (95 °C), 120–330 °C –1.0%, 330–395 °C –1.8% (372 °C), and 400–650 °C –5.2% (431 °C). **3**: 20–70 °C –0.8% (43 °C), 70–120 °C –3.7% (90 °C), 120–345 °C –1.0%, 345–415 °C –2.2% (380 °C), and 415–680 °C –5.8% (449 °C). **4**: 25–80 °C –1.1% (41 °C), 80–115 °C –3.7% (93 °C), 115–345 °C –1.1%, 350–390 °C –1.9% (366 °C), and 420–680 °C –5.6% (445 °C). **5**: 20–65 °C –0.9%, 65–105 °C –3.8% (81 °C), 105–350 °C –1.2% (188 °C), 350–400 °C –1.7% (374 °C), and 425–700 °C –4.3% (461 °C).

2.2. Instrumentation. Elemental analysis for carbon, hydrogen, and nitrogen was performed on an Exeter Analytical CE-440 Elemental Analyzer. Samples were combusted under an oxygen atmosphere at 975 °C for 1 min with helium used as the purge gas.

Attenuated total reflection Fourier transform infrared (ATR-FTIR) spectra (range 4000–100 cm^{-1}) were measured on a Matson 7000 FTIR spectrometer equipped with a Specac Golden Gate Mk II ATR Accessory having a diamond top plate and KRS-5 focusing lenses. Fourier transform Raman (FT Raman) spectra (range 4000–100 cm^{-1}) were recorded on a Bruker RFS 100 spectrometer with a Nd:YAG coherent laser ($\lambda = 1064 \text{ nm}$).

Thermogravimetric analyses (TGA) were carried out using a Shimadzu TGA 50, from room temperature to ca. 700 °C, with a heating rate of 5 °C/min under a continuous nitrogen stream with a flow rate of 20 cm^3/min .

Scanning electron microscopy (SEM) images and energy dispersive analysis of X-ray spectroscopy (EDS) studies were per-

formed in a Hitachi S-4100 field emission gun tungsten filament instrument working at 25 kV. Samples were prepared by deposition on aluminum sample holders and carbon coating.

Optical photographs were taken on a Stemi 2000 stereomicroscope equipped with Carl Zeiss lenses and a digital high-resolution AxioCam MRc5 digital camera connected to a personal computer.

Variable-temperature powder X-ray diffraction (VTPXRD) data for $[\text{Eu}(\text{H}_3\text{NMP})]\cdot 1.5\text{H}_2\text{O}$ were collected on a X'Pert MPD Philips diffractometer in a Bragg–Brentano para-focusing optics configuration (40 kV, 50 mA), equipped with curved graphite-monochromated radiation (Cu $\text{K}\alpha$ X-radiation, $\lambda = 1.54060 \text{ \AA}$), and a high-temperature Antoon Parr HKL 16 chamber, which was controlled by a Antoon Parr 100 TCU unit. Intensity data were collected in step mode (0.05° step) in the ca. $3 \leq 2\theta^\circ \leq 70$ angular range.

High-resolution synchrotron PXRD data for the crystal solution and refinement of $[\text{Pr}(\text{H}_3\text{NMP})]\cdot 1.5\text{H}_2\text{O}$ (**2**) were collected at ambient temperature (273 K) on the Swiss-Norwegian BM01b beam line (bending magnet source) at the European Synchrotron Radiation Facility (ESRF), Grenoble, France. The final Rietveld plot is depicted in Figure 1, and the final profile and reliability factors are collected in Table 1. Further details on the crystal solution and refinement from synchrotron PXRD data plus phase identification of $[\text{Ln}(\text{H}_3\text{NMP})]\cdot 1.5\text{H}_2\text{O}$ [$\text{Ln}^{3+} = \text{La}^{3+}$ (**1**), Nd^{3+} (**3**), Sm^{3+} (**4**), and Eu^{3+} (**5**)] using conventional PXRD data are provided as Supporting Information.

Detailed experimental information related to the solid-state NMR and photoluminescence studies described in the following paragraphs are also provided as Supporting Information.

3. Results and Discussion

3.1. Crystal Morphology. As-synthesized crystalline materials $[\text{Ln}(\text{H}_3\text{NMP})]\cdot 1.5\text{H}_2\text{O}$ [$\text{Ln}^{3+} = \text{La}^{3+}$ (**1**), Pr^{3+} (**2**), Nd^{3+} (**3**), Sm^{3+} (**4**), and Eu^{3+} (**5**)] exhibit an anisotropic lath-like crystal morphology as depicted in Figure 2, which prevented a priori structural analysis by single-crystal X-ray diffraction. PXRD patterns were systematically affected by textural effects, namely, strong preferential orientation as shown in the powder patterns given as Supporting Information for the materials with La^{3+} , Nd^{3+} , Sm^{3+} , and Eu^{3+} . Even though a reliable indexation was possible, *ab initio* structure solution systematically failed due to both systematic errors in the extraction of intensities of individual reflections and poor peak shape profile functions for reflections other than the first one (which is very intense and markedly asymmetric). The structure could only be elucidated from high-resolution synchrotron powder data of **2** with phase identification of the other materials being performed by CHN elemental and EDS analyses and PXRD (Le Bail profile fittings; see Supporting Information). Noteworthy, the multicompeting March–Dollase preferred orientation function¹⁶ employed in the structural refinement from synchrotron data strongly suggests a predominant growth of the crystallites along the [100] direction, with a refined parameter for the ratio of the effect along the latter axis with respect to that along the perpendicular plane *bc* of 0.661. These findings are in accord with the crystal habit revealed by SEM analyses (Figure 2).

3.2. Crystal Structure Description of $[\text{Ln}(\text{H}_3\text{NMP})]\cdot 1.5\text{H}_2\text{O}$. Structural studies using high-resolution synchrotron

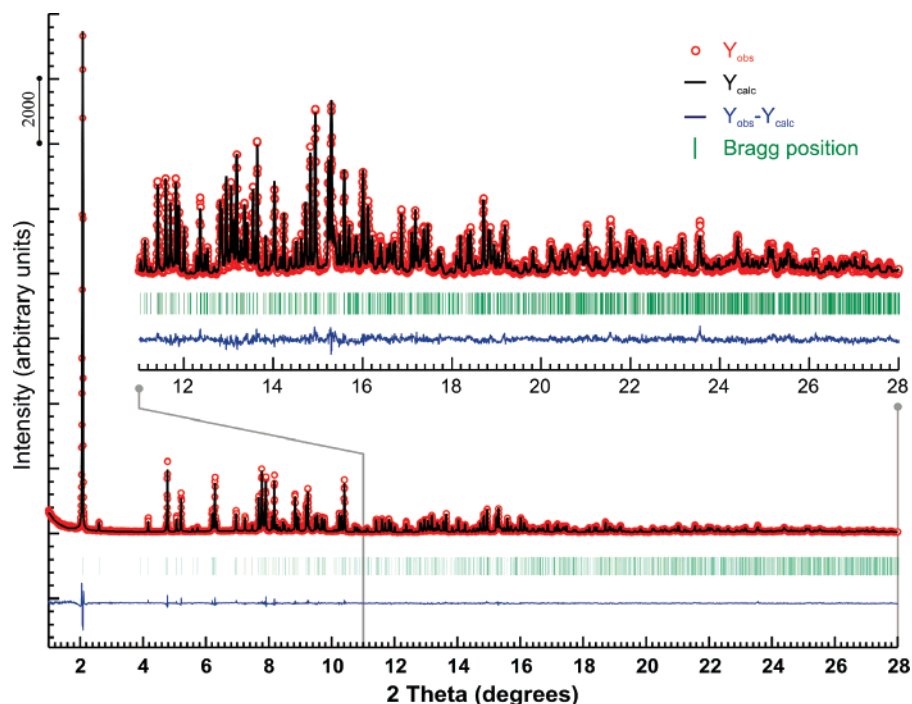


Figure 1. Final Rietveld plot (synchrotron PXRD data) of $[\text{Pr}(\text{H}_3\text{NMP})]\cdot 1.5\text{H}_2\text{O}$. Observed data points are indicated as red circles; the best-fit profile (upper trace) and the difference pattern (lower trace) are drawn as solid black and blue lines, respectively. Green vertical bars indicate the angular positions of the allowed Bragg reflections.

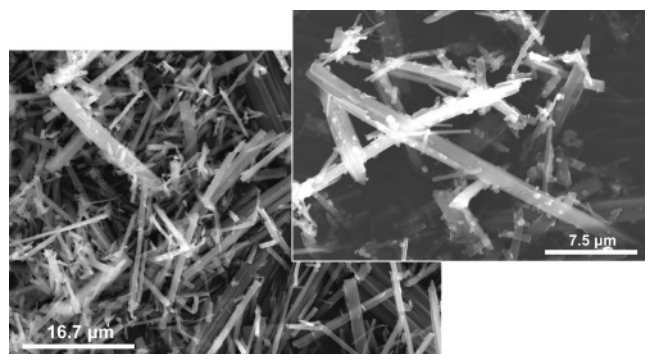


Figure 2. Scanning electron microscopy images of $[\text{Nd}(\text{H}_3\text{NMP})]\cdot 1.5\text{H}_2\text{O}$ (bottom) and $[\text{Pr}(\text{H}_3\text{NMP})]\cdot 1.5\text{H}_2\text{O}$ (top).

PXRD data of **2** and information from solid-state NMR of **1** revealed layered materials built up from Ln^{3+} centers and bridging $\text{H}_3\text{NMP}^{3-}$ ligands. Materials **1–5** are isostructural, crystallizing in the orthorhombic space group *Pbcn*. Since geometrical parameters could only be unequivocally determined for **2**, relevant structural details will be focused on this material.

The asymmetric unit of $[\text{Pr}(\text{H}_3\text{NMP})]\cdot 1.5\text{H}_2\text{O}$ consists of one eight-coordinated Pr^{3+} metal center, one bridging and chelating $\text{H}_3\text{NMP}^{3-}$ anionic ligand, and two uncoordinated water molecules (Figure 3). The crystallographic unique Pr^{3+} cation is coordinated by eight phosphonate oxygen atoms from four symmetry-related $\text{H}_3\text{NMP}^{3-}$ anionic ligands, $\{\text{PrO}_8\}$, in a highly distorted dodecahedral coordination geometry: while the Pr–O bond lengths were found in the 2.343(3)–2.582(4) Å range, comparable to those reported for other Pr^{3+} -containing phosphonate materials (CSD, 12 entries, bond lengths in the 2.32–2.77 Å range with median of 2.45 Å), the internal O–Pr–O polyhedral angles are in the 56.10(10)–148.55(10)° range (Table 2). It is important

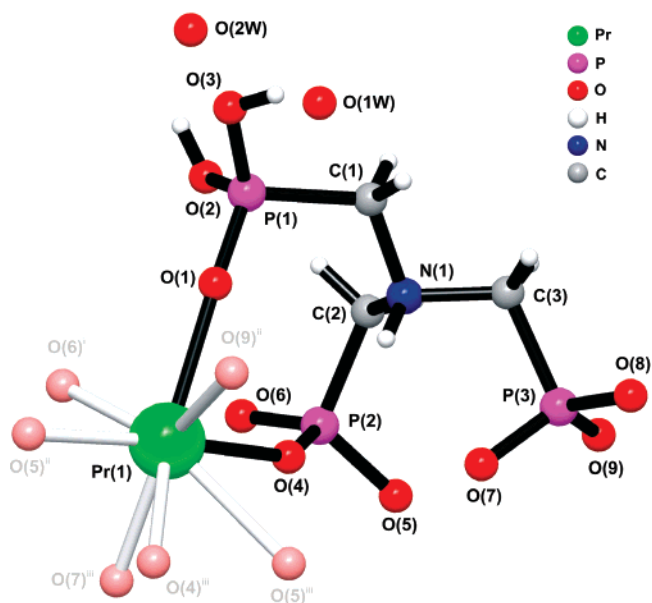


Figure 3. Ball-and-stick representation of asymmetric unit and coordination environment in $[\text{Pr}(\text{H}_3\text{NMP})]\cdot 1.5\text{H}_2\text{O}$ showing the labeling scheme for all non-hydrogen atoms. For selected bond lengths and angles see Table 2. Symmetry transformations used to generate symmetry-equivalent atoms: (i) $x, -y, 1/2 + z$; (ii) $x, y, 1 + z$; (iii) $1.5 - x, 1/2 - y, 1/2 + z$.

to note that even though the materials were synthesized in aqueous media and water is present in the crystal structure of **2**, the first coordination sphere of Pr^{3+} is water free. This relatively uncommon structural feature among MOFs (particularly 2D) has an impact on the photoluminescence properties of the material (see below).

The detailed structural features associated with the $\text{H}_3\text{NMP}^{3-}$ anionic ligand, in particular the location of the protonating hydrogen atoms, could only be fully determined when information from the solid-state NMR studies was taken into

Table 1. X-ray Data Collection, Crystal Data, and Structure Refinement Details for [Pr(H₃NMP)]·1.5H₂O

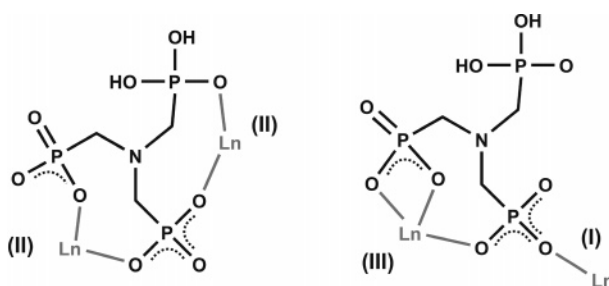
diffractometer	data collection	
wavelength (Å)	BM01b beam line; ESRF, France	
temp. (K)	0.50018(1)	
geometry	293	
2θ range (deg)	Debye–Scherrer	
step size (deg)	0.732–28.000	
	0.004	
formula	unit cell	
fw	C ₆ H ₁₈ N ₂ O ₂₁ Pr ₂	
cryst syst	921.86	
space group	orthorhombic	
a/Å	Pbcn	
b/Å	27.5001(4)	
c/Å	11.99777(18)	
V/Å ³	7.25373(11)	
Z	2393.30(6)	
D _c /g cm ^{−3}	4	
	2.558	
profile function	profile parameters	
Caglioti law parameters	split pseudo-Voigt	
	U _r = 0.006(2)	U _l = 0.041(2)
	V _r = 0.0011(4)	V _l = −0.0070(3)
	W _r = 0.00033(1)	W _l = 0.00062(1)
	η _r = 0.39(1)	
asymmetry parameters (up to 20° 2θ)	0.0090(6) and 0.0020(2)	
zero point	−0.0026(2)	
multiaxial March–Dollase	[100]: G = 1.05(1); fraction = 0.661	
	[011]: G = 0.86(6)	
	refinement details	
no. of independent reflections	1185	
no. of global refined parameters	1	
no. of profile refined parameters	16	
no. of intensity-dependent refined parameters	7	
	reliability factors for points with Bragg contribution (conventional, not corrected for background)	
R _p	7.81	
R _{wp}	10.49	
R _{exp}	8.23	
χ ²	1.62	
	structure reliability factors	
R _{Bragg}	5.64	
R _F	6.32	
CCDC deposition number	638590	

Table 2. Selected Bond Lengths (in Å) and Angles (in deg) for the Pr³⁺ Coordination Environment Present in [Pr(H₃NMP)]·1.5H₂O^a

Pr(1)–O(1)	2.429(3)	Pr(1)–O(5) ⁱⁱ	2.416(4)
Pr(1)–O(4)	2.479(3)	Pr(1)–O(6) ⁱⁱⁱ	2.343(3)
Pr(1)–O(4) ⁱ	2.581(4)	Pr(1)–O(7) ⁱ	2.414(3)
Pr(1)–O(5) ⁱ	2.582(4)	Pr(1)–O(9) ⁱⁱ	2.499(4)
O(1)–Pr(1)–O(4)	78.94(11)	O(6) ⁱⁱⁱ –Pr(1)–O(4)	92.20(13)
O(1)–Pr(1)–O(4) ⁱ	138.55(12)	O(6) ⁱⁱⁱ –Pr(1)–O(4) ⁱ	132.50(13)
O(1)–Pr(1)–O(5) ⁱ	118.65(14)	O(6) ⁱⁱⁱ –Pr(1)–O(5) ⁱ	144.71(11)
O(1)–Pr(1)–O(9) ⁱⁱ	66.07(13)	O(6) ⁱⁱⁱ –Pr(1)–O(5) ⁱⁱ	78.60(11)
O(4)–Pr(1)–O(4) ⁱ	119.19(9)	O(6) ⁱⁱⁱ –Pr(1)–O(7) ⁱ	78.80(11)
O(4)–Pr(1)–O(5) ⁱ	63.95(12)	O(6) ⁱⁱⁱ –Pr(1)–O(9) ⁱⁱ	132.21(13)
O(4)–Pr(1)–O(9) ⁱⁱ	109.72(13)	O(7) ⁱ –Pr(1)–O(1)	148.55(11)
O(4) ⁱ –Pr(1)–O(5) ⁱ	56.10(10)	O(7) ⁱ –Pr(1)–O(4)	81.05(12)
O(5) ⁱⁱ –Pr(1)–O(1)	105.07(14)	O(7) ⁱ –Pr(1)–O(4) ⁱ	72.77(12)
O(5) ⁱⁱ –Pr(1)–O(4)	168.77(12)	O(7) ⁱ –Pr(1)–O(5) ⁱ	72.34(12)
O(5) ⁱⁱ –Pr(1)–O(4) ⁱ	64.80(12)	O(7) ⁱ –Pr(1)–O(5) ⁱⁱ	90.75(12)
O(5) ⁱⁱ –Pr(1)–O(5) ⁱ	120.90(9)	O(7) ⁱ –Pr(1)–O(9) ⁱⁱ	144.50(12)
O(5) ⁱⁱ –Pr(1)–O(9) ⁱⁱ	81.40(14)	O(9) ⁱⁱ –Pr(1)–O(4) ⁱ	72.58(12)
O(6) ⁱⁱⁱ –Pr(1)–O(1)	77.99(12)	O(9) ⁱⁱ –Pr(1)–O(5) ⁱ	82.17(14)

^a Symmetry transformations used to generate equivalent atoms: (i) 1/2 − x, 1/2 − y, 1/2 + z; (ii) x, y, 1 + z; (iii) x, −y, 1/2 + z.

account (see following section). While P(1) remains fully protonated (−PO₃H₂), the remaining two crystallographically independent phosphonate groups, P(2) and P(3), are fully deprotonated (−PO₃^{2−}). Moreover, the central amine functional group is also protonated (Figure 3). This zwitterionic behavior of H₃NMP^{3−} is not unprecedented among amino–phosphonate-type compounds, as revealed by a search in the Cambridge Structural Database.¹⁷

Scheme 1. Coordination Modes of the H₃NMP^{3−} Anionic Ligand in [Pr(H₃NMP)]·1.5H₂O (2). Bonds to the Metal Centers Are Drawn in Gray

H₃NMP^{3−} acts as an octadentate ligand, establishing a single unidentate interaction (mode I; Scheme 1), two chelate bidentate interactions, each involving two different phosphonate groups with two symmetry-related lanthanide centers (mode II; Scheme 1), plus one chelate tridentate interaction with one Pr³⁺ center and involving two phosphonate groups from the same anionic H₃NMP^{3−} residue (mode III; Scheme 1). In fact, such high connectivity associated with the anionic chelating residues traps Pr³⁺ inside a phosphonic-type inorganic matrix, leading to a sterically hindered environ-

(17) Allen, F. H. *Acta Crystallogr., Sect. B* **2002**, 58, 380–388. Allen, F. H.; Motherwell, W. D. S. *Acta Crystallogr., Sect. B* **2002**, 58, 407–422.

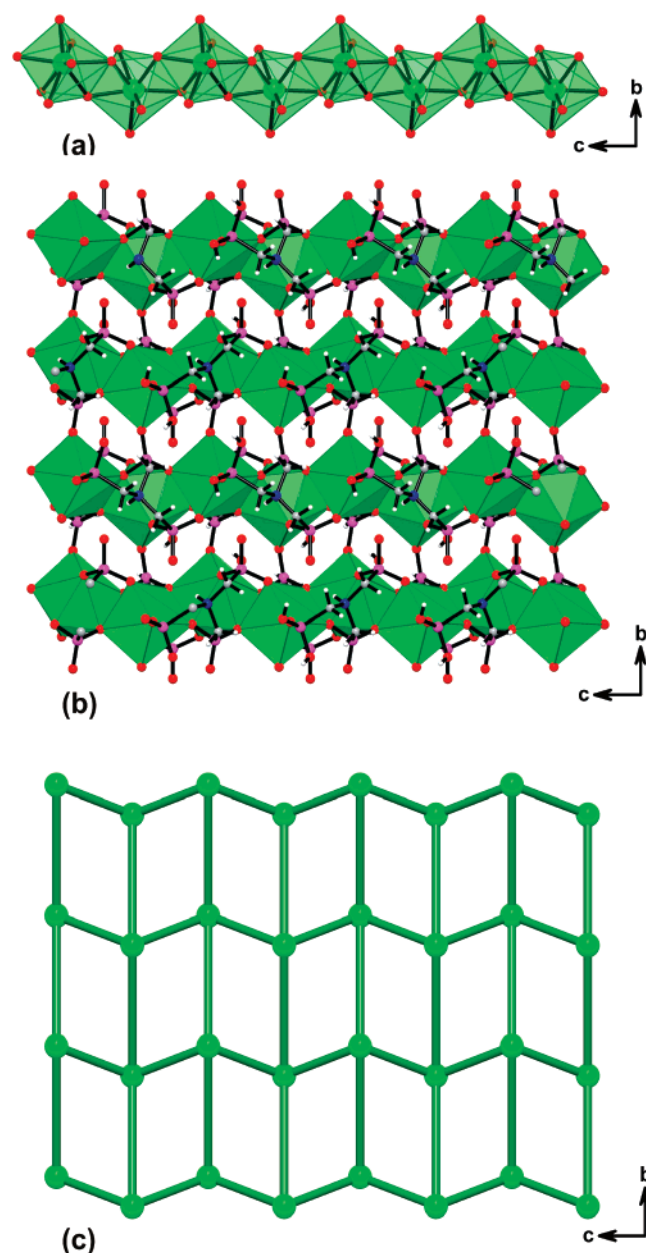


Figure 4. (a) 1D inorganic backbone, running parallel to the *c* axis of the unit cell and built-up from edge-shared praseodymium oxide highly distorted dodecahedra, {PrO₈}. (b) Mixed ball-and-stick and polyhedral representation of the 2D LnOF ∞^2 [Pr(H₃NMP)] and its (c) (4,4) topological representation viewed toward the *bc* plane of the unit cell. Color scheme as in Figure 3.

ment, which prevents inclusion of water molecules in the first coordination sphere.

The crystal structure of **2** possesses a one-dimensional (1D) inorganic backbone running along the [001] direction of the unit cell and built up from edge-shared {PrO₈} polyhedra (Figure 4a). The closest intrachain Pr(1)⋯Pr(1)ⁱ distance is 4.2384(1) Å, arising from the chelation fashion III described above [symmetry code: (i) 1.5 − *x*, 1/2 − *y*, −1/2 + *z*]. Interchain connections along the [010] direction are assured by the bridging deprotonated phosphonate groups (mode I; Scheme 1), imposing a Pr(1)⋯Pr(1)ⁱⁱ intermetallic distance of 6.2398(1) Å [symmetry code: (ii) 1.5 − *x*, 1/2 + *y*, *z*]. This leads to the formation of a neutral undulated 2D LnOF, ∞^2 [Pr(H₃NMP)] (Figure 4b), placed in the *bc* plane of the unit cell. Taking the metal centers as central nodes, this

Table 3. Hydrogen-Bonding Geometry (distances in Å and angles in deg) for [Pr(H₃NMP)]·1.5H₂O^a

D—H⋯A	<i>d</i> (D⋯A)	<(DHA)
O(2)—H(2)⋯O(2W)	2.555(5)	128(5)
O(3)—H(3)⋯O(1W)	2.767(7)	136(7)
N(1)—H(1)⋯O(8) ^{iv}	2.997(6)	137(4)
N(1)—H(1)⋯O(4)	2.923(6)	114(4)
N(1)—H(1)⋯O(7)	2.784(6)	111(3)
O(1W)⋯O(1W) ^v	2.682(9)	
O(2W)⋯O(3) ^{vi}	2.602(6)	

^a Symmetry transformations used to generate equivalent atoms: (iv) *x*, 1 − *y*, 1/2 + *z*; (v) 1 − *x*, +1 + *y*, 1 − *z*; (vi) 1 − *x*, −*y*, 1 − *z*.

network can thus topologically be described as a (4,4) plane net, with the shortest possible circuit being a rectangle with the internodal dimensions given above.¹⁸

It is important to note that the structural cohesion within this ∞^2 [Pr(H₃NMP)] plane net is further assured by N⁺—H⋯O hydrogen-bonding interactions involving the protonated amine and neighboring oxygen atoms. Indeed, three interactions are chemically feasible (Table 3 and Figure S5 in the Supporting Information). Even though the reported <(DHA) interaction angles do not approach linearity, it is fair to assume that in the crystal structure the true position of the protonating hydrogen atom will be such that it maximizes hydrogen bonding, with the reported position being just an average spatial value (hence the low interaction angles).

Individual ∞^2 [Pr(H₃NMP)] networks close pack along the [100] direction in a typical ABAB⋯ fashion with adjacent layers related by inversion (Figure 5a). Interlayer spaces are filled up with water molecules of crystallization, which are engaged in a series of hydrogen-bonding interactions (Figure 5 and Table 3). In addition to the N⁺—H⋯O intralayer hydrogen bonds aforementioned, the protonated P—OH groups of the ∞^2 [Pr(H₃NMP)] layer donate their hydrogen atoms to two neighboring and crystallographically independent water molecules of crystallization: P—O(2)—H⋯O(2W) and P—O(3)—H⋯O(1W) with D⋯A distances of 2.555(5) and 2.767(7) Å, respectively. Besides donating its hydrogen atom to O(1W), O(3) also acts as an acceptor in an interaction involving O(2W) (Table 3). Moreover, the water molecules O(1W) reside in a small 1D channel formed by the close packing of individual layers (Figure 5a). This leads to formation of a spiral 1D-confined water cluster running parallel to the *c* axis with a O(1W)⋯O(1W)ⁱⁱⁱ distance of 2.682(9) Å [symmetry code: (iii) 1 − *x*, −1 + *y*, 1 − *z*]. This water cluster interacts directly with adjacent ∞^2 [Pr(H₃NMP)] layers via the stabilizing P—O(3)—H⋯O(1W) hydrogen bonds mentioned above. The full graph set motif of the hydrogen-bonding subnetwork depicted in Figure 5c (and Figure S6 in the Supporting Information) is C(3)R₅⁵(10)S-(3)S(3).¹⁹

3.3. Solid-State NMR. The ¹³C CPMAS spectrum (Figure 6a) reveals the presence of several peaks arising due to the indirect dipole—dipole couplings between ³¹P and ¹³C nuclei (²*J*_{C—P}). ¹³C observation employing ³¹P decoupling during

(18) Wells, A. F. *Structural Inorganic Chemistry*, 4th ed.; Clarendon Oxford University Press: New York, 1975.

(19) Bernstein, J.; Davis, R. E.; Shimon, L.; Chang, N. L. *Angew. Chem., Int. Ed. Engl.* **1995**, *34*, 1555–1573.

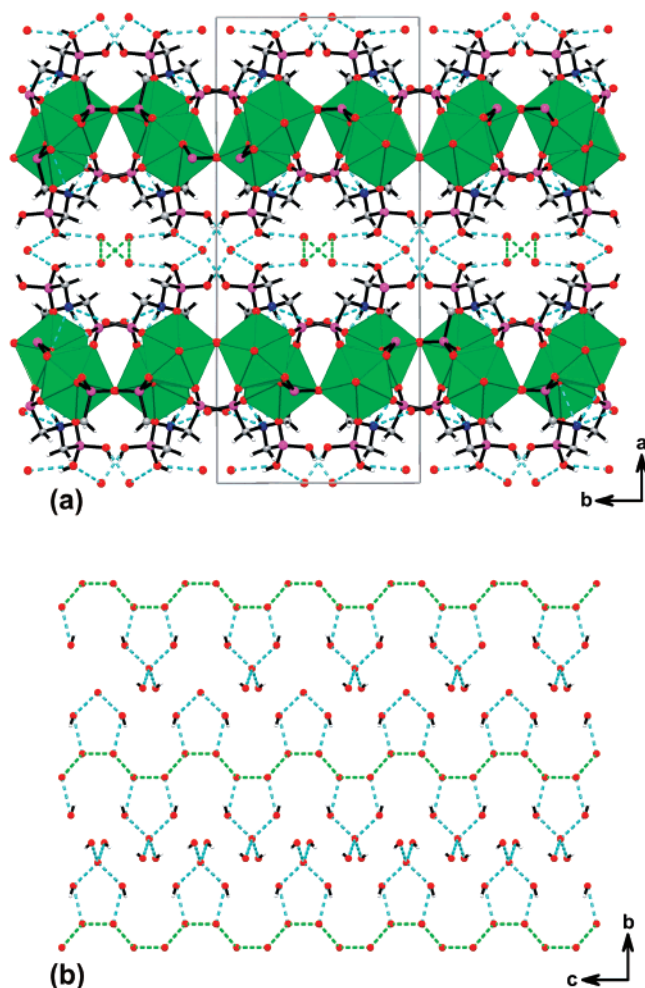


Figure 5. (a) Crystal packing of $[\text{Pr}(\text{H}_3\text{NMP})]\cdot 1.5\text{H}_2\text{O}$ (**2**) viewed along the $[001]$ direction of the unit cell. Hydrogen bonds are represented as dashed lines. (b) Hydrogen-bonding subnetwork involving the water molecules of crystallization. Water-to-water interactions are represented as light-green dashed bonds, while interactions between water and the $\infty^2[\text{Pr}(\text{H}_3\text{NMP})]$ layers are drawn as light-blue dashed lines. For geometrical details on the hydrogen bonds see Table 3 and Figure S6 (Supporting Information). Color scheme as in Figure 3.

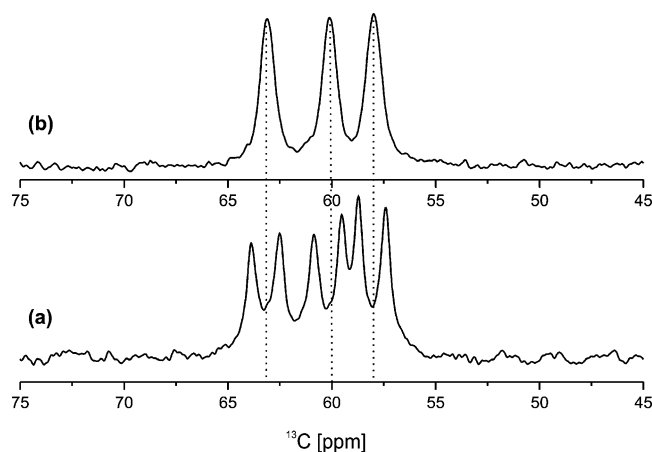


Figure 6. ^{13}C CPMAS spectra of $[\text{La}(\text{H}_3\text{NMP})]\cdot 1.5\text{H}_2\text{O}$ (a) without and (b) with ^{31}P decoupling during the acquisition period.

the detection period (Figure 6b) reveals three crystallographically distinct carbon sites per unit cell, resonating at ca. 63, 60, and 58 ppm, in ca. 1:1:1 population ratios. This is in accord with the crystal model refined from powder X-ray data. Moreover, as expected, the ^{15}N CPMAS spectrum

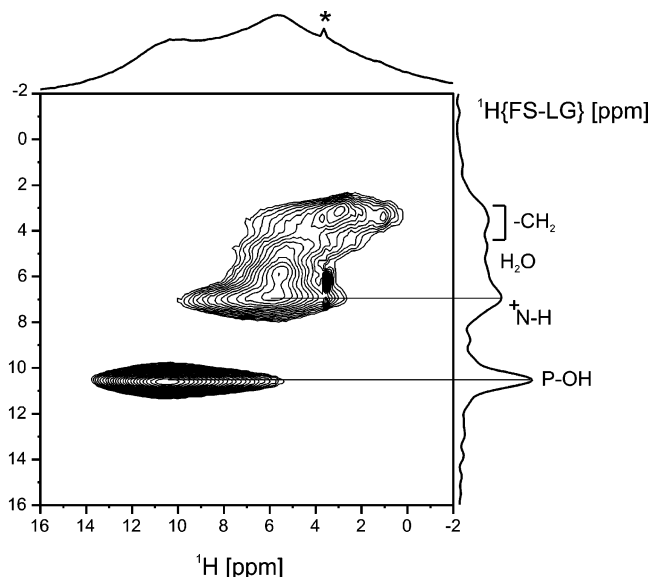


Figure 7. Contour plot of a 2D $^1\text{H}\{\text{FS-LG}\}-^1\text{H}$ HOMCOR spectrum of $[\text{La}(\text{H}_3\text{NMP})]\cdot 1.5\text{H}_2\text{O}$. The asterisk depicts an impurity.

(Figure S7 in the Supporting Information) displays a single peak at -330 ppm, which is in the range of zwitterionic aminophosphonic chemical shifts.²⁰

The $^1\text{H}\{\text{FS-LG}\}-^1\text{H}$ HOMCOR spectrum (Figure 7) is well resolved, providing useful information on the ^1H chemical environments of **1**: the resonances between 3 and 4 ppm are attributed to $-\text{CH}_2-$ groups; those between 4.5 and 6.0 ppm may be assigned to hydrogen-bonded or free water molecules; the resonance at ca. 7.0 ppm is typical of protonated amines ($^+\text{N}-\text{H}$);²¹ the sharp peak at ca. 10.5 ppm indicates the presence of acidic protons, clearly supporting the presence of $\text{P}-\text{OH}$ groups. The ^1H resonances of aminophosphonic $\text{P}-\text{OH}$ groups typically appear above 10 ppm.²² In short, this 2D NMR spectrum provides strong evidence for (i) protonation of the central nitrogen atom of the $\text{H}_{6-x}\text{NMP}^{-x}$ residue (ca. 7.0 ppm) and (ii) the presence of protonated phosphonate groups, possibly involved in hydrogen bonds (ca. 10.5 ppm).

The 2D $^1\text{H}\{\text{FS-LG}\}-^{31}\text{P}$ HETCOR spectra (Figure 8) provide information on which phosphonate group is protonated and engaged in hydrogen bonds. For a contact time (CT) of 1 ms all $^1\text{H}-^{31}\text{P}$ dipolar cross-peaks are completely correlated due to ^1H spin diffusion during the mixing time (Figure 8a). Decreasing the CT from 1 ms to 100 μs the cross-peaks of the ^1H resonances in the 3–7 ppm region become weaker than the ^1H resonance at ca. 10.5 ppm (Figure 8b). However, a 100 μs CT does not afford enough selectivity. Hence, off-resonance (LG-CP) spin lock was used to quench spin diffusion during the CP (Figure 8c). The ^1H spins are decoupled during CP, allowing higher selectivity, even when relatively long CTs are used. The cross-peaks of the 3–7 ppm ^1H resonances disappear almost completely with only the cross-peak involving the $\text{P}-\text{OH}$ ^1H resonances

(20) Harris, R. K.; Merwin, L. H.; Hagele, G. *Magn. Reson. Chem.* **1989**, 27, 470–475.

(21) Mafra, L.; Paz, F. A. A.; Rocha, J.; Espina, A.; Khainakov, S. A.; Garcia, J. R.; Fernandez, C. *Chem. Mater.* **2005**, 17, 6287–6294.

(22) Harris, R. K.; Jackson, P.; Merwin, L. H.; Say, B. J.; Hagele, G. *Faraday Trans.* **1988**, 84, 3649–3672.

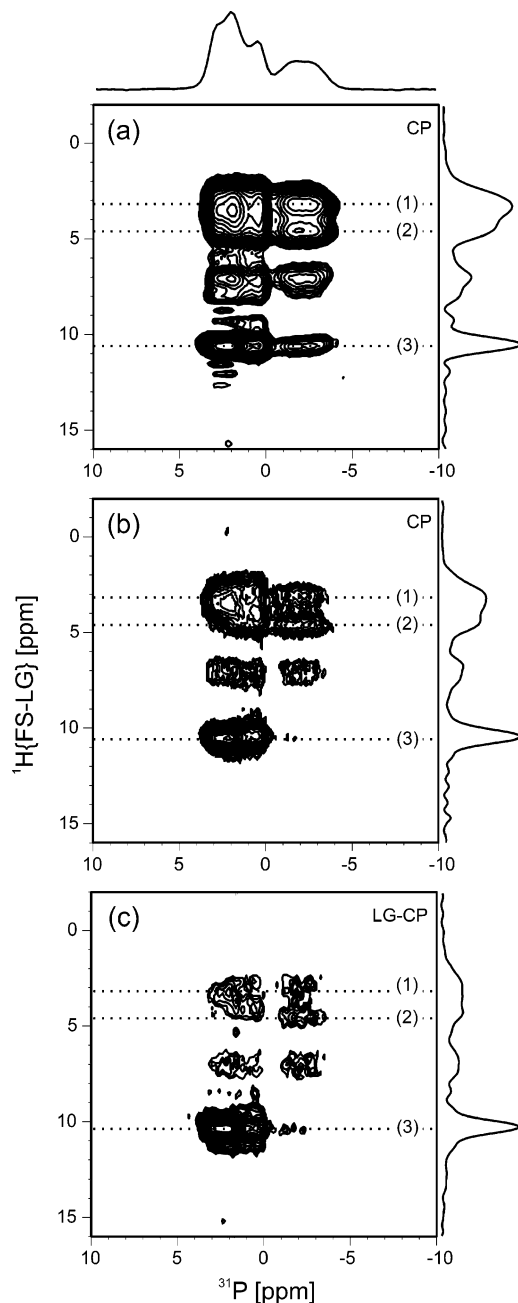


Figure 8. 2D $^1\text{H}\{\text{FS-LG}\}-^{31}\text{P}$ HETCOR NMR spectra of $[\text{La}(\text{H}_3\text{NMP})]\cdot 1.5\text{H}_2\text{O}$ employing CP with CT of (a) 1 ms and (b) 100 μs and (c) LG-CP with CT of 1 ms. The horizontal dotted lines 1, 2, and 3 depict F2 cross-sections taken at the ^1H 3.2, 4.8, and 10.5 ppm, respectively, and shown in Figure S8 (Supporting Information).

and the ^{31}P resonances above 0 ppm being present. The intensities of the peaks in the F2 slices of the spectra in Figure 8a–c were compared (Figure S8a–c in the Supporting Information). Use of off-resonance CP (CT of 1 ms) (Figure 8c, solid lines in Figure S8) affords even better spectral discrimination and, as detailed in the following paragraphs, shows that not all the phosphorus sites contain OH groups. For example, the ^{31}P peak at ca. –2 ppm decreases considerably, while the peak at ca. 0.5 ppm becomes faint in the 2D LG-CP spectrum of Figure 8c (compare Figures 8a–c plus solid lines in Figure S8), showing that the ca. 2.8 ppm resonance (and its shoulder at ca. 1.9; Figure 4c) remains strongly cross-polarized with respect to the other ^{31}P resonances. This suggests that two P–OH groups, with

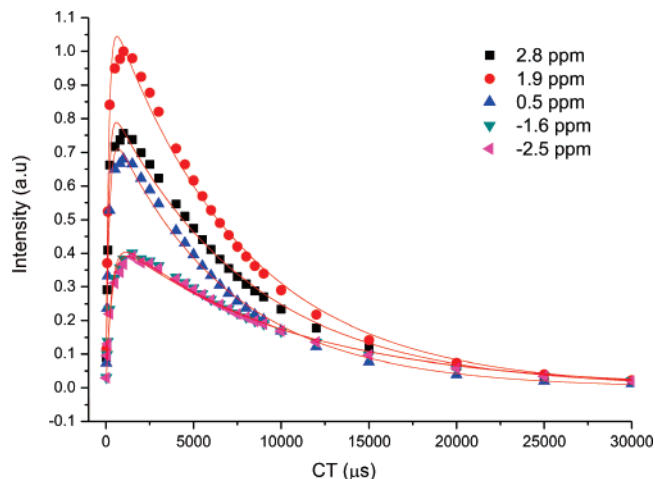


Figure 9. Evolution of signal intensities of the selected groups of nitrilotris-(methylphosphonic acid) residues as a function of the contact time. All ^{31}P curves were fitted using the classical kinetic model.

similar environments but crystallographically distinct, are involved in hydrogen bonds with water molecules. However, this is in conflict with the PXRD structure, according to which the two P–OH groups are part of the same phosphonate group. The ^{31}P spectrum displays more than three ^{31}P peaks, which, at first sight, does not seem to be in accord with the PXRD structure and is also difficult to reconcile with the $^{13}\text{C}/^{15}\text{N}$ CPMAS NMR results. This is likely to be due to the indirect $^{31}\text{P}-^{139}\text{La}$ dipole–dipole couplings (P–O–La bonds), as observed in other systems such as aluminophosphates.²³ Indeed, spectral integration yields a ratio of ca. 2:1 for, respectively, the resonances in the 0–4 ppm range and the broad peak at ca. –2 ppm, indicating that three crystallographically distinct ^{31}P sites are present.

More information on the assignment of the ^{31}P resonances may be obtained from study of the $^1\text{H}-^{31}\text{P}$ CP dynamics. In particular, build-up CP times, T_{CH} and T_{PH} , and rotating frame spin–lattice relaxation times, $T_{1\rho}^{\text{H}}$, may be extracted from the fitting of the CP kinetic curves (Figure 9) assuming the classical model,²⁴ valid for weak heteronuclear dipolar couplings:

$$I(t) = I_0 \left(1 - \frac{T_{\text{IS}}}{T_{1\rho}^{\text{I}}} \right)^{-1} \left[\exp\left(\frac{-t}{T_{1\rho}^{\text{I}}} \right) - \exp\left(\frac{-t}{T_{\text{IS}}} \right) \right]$$

The magnitude of T_{PH} is determined by the molecular mobility and dipolar couplings because the distance between ^{31}P and ^1H spins is, to a first approximation, proportional to $(T_{\text{PH}})^{-6}$.²⁵ Assuming equal mobility among the phosphorus domains, analysis of the cross-polarization times (T_{PH}) allows a comparison of the average $^{31}\text{P}\cdots^1\text{H}$ distances, providing structural information on the protonation of the phosphonate groups. After the initial rapid build up of the ^{31}P magnetization, the phosphorus signal tracks the polarization in the proton reservoir and follows its decrease via $T_{1\rho}^{\text{I}}$ ($I = ^1\text{H}$) relaxation. Five ^{31}P peaks were selected to obtain the kinetic

(23) Fyfe, C. A.; Altmenschilde, H. M. Z.; Wong-Moon, K. C.; Grondy, H.; Chezeau, J. M. *Solid State Nucl. Magn. Reson.* **1997**, *9*, 97–106.

(24) Kolodziejewski, W.; Klinowski, J. *Chem. Rev.* **2002**, *102*, 613–628.

(25) Douwel, C. H. K.; Maas, W. E. J. R.; Veenman, W. S.; Buning, G. H. W.; Vankan, J. M. *J. Macromolecules* **1990**, *23*, 406–412.

Table 4. Dynamic Parameters Obtained by Fitting the CP Kinetic Data for Selected ^{31}P Chemical Shifts of the ^{31}P CPMAS Spectrum

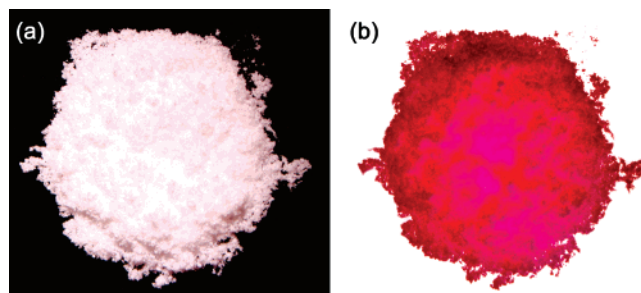
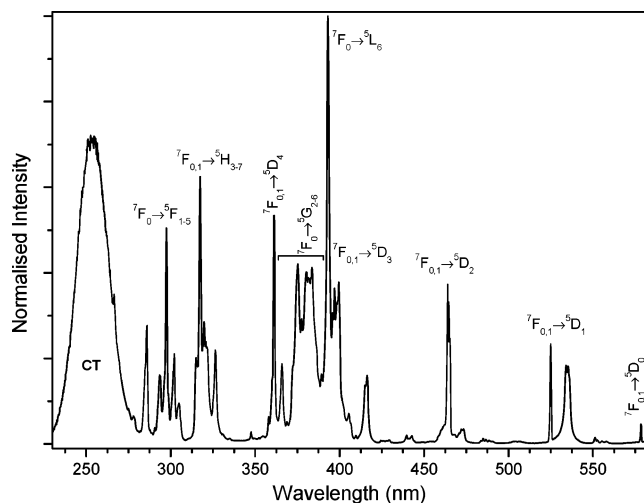
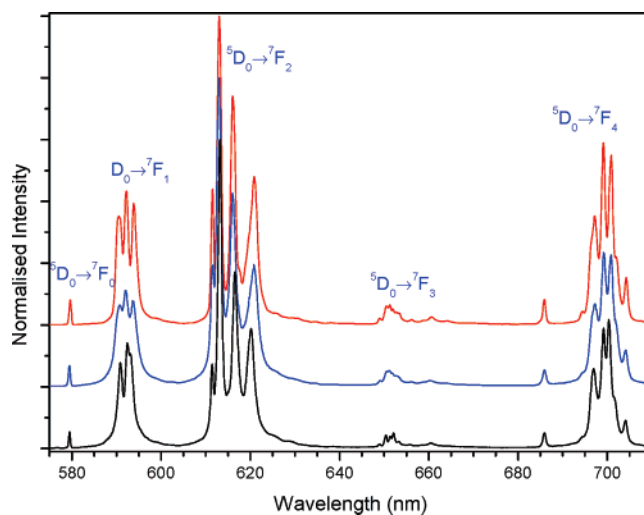
peaks [ppm]	T_{PH} (μs)	$T_{1\rho}^{\text{H}}$ (ms)
2.8	145.3 ± 7.2	8.0 ± 0.2
1.9	157.5 ± 7.8	7.6 ± 0.2
0.5	184.0 ± 8.6	6.8 ± 0.2
−1.6	322.4 ± 19.5	10.2 ± 0.4
−2.5	342.0 ± 21.2	10.4 ± 0.4

information collected in Table 4 (T_{PH} and $T_{1\rho}^{\text{H}}$). The broad ^{31}P resonance at ca. −2 ppm has two components (at ca. −1.6 and −2.5 ppm) with almost identical relaxation parameters, which supports the assumption that this peak is not the superposition of two ^{31}P resonances but arises from the J -coupling interaction between ^{31}P and ^{139}La . The T_{PH} values of the ^{31}P resonances above 0 ppm are shorter (approximately one-half) than the value of the peak at negative chemical shift, thus suggesting that the former sites are close in space to ^1H nuclei (excluding the $-\text{CH}_2$ group, which is common to all sites). The slightly larger T_{PH} value of the ^{31}P signal at ca. 0.5 ppm, when compared to the ^{31}P peaks at ca. 1.9 and 2.8 (shoulder) ppm, suggests that the former corresponds to the phosphorus site containing a single ^1H nucleus in its surroundings. The most likely candidate is the site with a $\text{P}=\text{O}$ terminal group hydrogen bonded to the protonated central nitrogen atom (Table 3 and Figure S5). Indeed, the F2 cross-section (Figure S8c, Supporting Information, solid line) of the 2D $^1\text{H}\{\text{FS-LG}\}-^{31}\text{P}$ HETCOR (Figure 8) shows that the ^{31}P resonance at ca. 0.5 ppm is still being polarized, albeit to a lower extent relatively to the ^{31}P peaks at ca. 1.9 and 2.8 ppm. The two latter resonances are assigned to the site containing the largest number of ^1H nuclei surrounding the oxygen atoms coordinated to the central phosphorus. This ultimately corresponds to the phosphorus site having two attached OH groups further involved in hydrogen-bonding interactions with two water molecules (see discussion concerning the hydrogen-bonding subnetwork present in the crystal structure).

The degree of coordination to lanthanum of each phosphorus site may also be deduced from the chemical shift of the ^{31}P resonances. The ^{31}P CPMAS spectrum (not shown) of nitrilotris(methylphosphonic acid) shows three ^{31}P resonances, at ca. 12.1 ppm, in a more deshielded region than that of **1**. This indicates that coordination to La^{3+} increases the chemical shielding. Thus, the assignment of the ^{31}P resonance at ca. −2 ppm to the site P(2), which has three La^{3+} next-nearest neighbors, is in accord with the CP kinetics results ($T_{\text{PH}} = 322\text{--}342 \mu\text{s}$). The ^{31}P resonance at ca. 0.5 ppm is assigned to P(3) (bound to two La^{3+} ; $T_{\text{PH}} = 184 \mu\text{s}$), while the remaining peak is given by P(1) (bound to a single La^{3+} , $T_{\text{PH}} = 145\text{--}157 \mu\text{s}$).

3.4. Photoluminescence. $[\text{Eu}(\text{H}_3\text{NMP})]\cdot 1.5\text{H}_2\text{O}$ (**5**) showed an intense red photoluminescence when irradiated with UV radiation (Figure 10).

The excitation spectrum of $[\text{Eu}(\text{H}_3\text{NMP})]\cdot 1.5\text{H}_2\text{O}$ recorded at room temperature (Figure 11) displays a series of sharp lines assigned to the $^7\text{F}_{0,1} \rightarrow ^5\text{D}_{4-0}$, $^5\text{L}_6$, $^5\text{G}_{2-6}$, $^5\text{H}_{3-7}$, and $^5\text{F}_{1-5}$ Eu^{3+} intra- $4f^6$ transitions. On the high-energy region, the spectrum exhibits an additional broad band, peaking at 253.5 nm, and attributed to ligand-to- Eu^{3+} charge transfer. The energy (4.89 eV) and full-width-at-half-maximum (0.36

**Figure 10.** Optical photographs of microcrystalline powder of $[\text{Eu}(\text{H}_3\text{NMP})]\cdot 1.5\text{H}_2\text{O}$ under (a) natural light and (b) ultraviolet irradiation (using a portable UV led with wavelength in the 375–380 range and power output of ca. 2 mW).**Figure 11.** Excitation spectrum of $[\text{Eu}(\text{H}_3\text{NMP})]\cdot 1.5\text{H}_2\text{O}$ recorded at room temperature. The emission was monitored at 613 nm.**Figure 12.** Emission spectra of $[\text{Eu}(\text{H}_3\text{NMP})]\cdot 1.5\text{H}_2\text{O}$ recorded at room temperature without vacuum (black line) and with high vacuum (blue line), and at 10 K (red line). The excitation was performed at 393 nm.

eV) of this charge-transfer band are in good agreement with the values reported for structures containing Eu^{3+} .²⁶

Figure 12 shows the emission spectra of $[\text{Eu}(\text{H}_3\text{NMP})]\cdot 1.5\text{H}_2\text{O}$ excited at 393 nm. The sharp lines are assigned to transitions between the first excited nondegenerate $^5\text{D}_0$ state and the $^7\text{F}_{0-4}$ levels of the fundamental Eu^{3+} septet. Except for the $^5\text{D}_0 \rightarrow ^7\text{F}_1$ lines, which have a predominant magnetic

dipole character, the observed transitions are mainly of electric dipole nature. The presence of one 5D_0 – 7F_0 line and the local-field splitting of the $^7F_{0,1,2}$ levels into three and a maximum of five Stark components, respectively, supports the structural evidence of a single low-symmetry Eu^{3+} environment, as indicated by the PXRD studies (see above). At room temperature exposure of the sample to a high vacuum (ca. 10^{-3} – 10^{-4} $\text{N}\cdot\text{m}^{-2}$) induces a broadening of the $^5D_0 \rightarrow ^7F_{0-4}$ lines and an increase on the maximum splitting of the $^5D_0 \rightarrow ^7F_{1,2}$ transitions [$\Delta E(^7F_i)$],⁴¹ more evident for the 7F_1 level (Figure 12) for which $\Delta E(^7F_1)$ increases from ca. 63 to 86 cm^{-1} . This maximum splitting is associated with the overall electrostatic energy of the Eu^{3+} local environments, illustrating therefore the differences between the covalency of the corresponding Eu–O bonds.²⁷ The increase in $\Delta E(^7F_1)$ with exposure to high vacuum is most likely associated with loss of the crystallization water molecules located in the interlayer space, suggesting a reduction in the covalent character of the Eu^{3+} local environment. The slight increase of the fwhm of the $^5D_0 \rightarrow ^7F_0$ line after vacuum exposure (from ca. 10.9 ± 0.1 to 13.1 ± 0.1 cm^{-1}) indicates that loss of the crystallization water molecules increases the nonhomogeneity of the Eu^{3+} -local coordination site (larger distribution of closely similar Eu^{3+} sites). This is in agreement with the suggestion that vacuum exposure reduces, on average, the covalency of the Eu–O bonds.

The 5D_0 lifetime of Eu^{3+} was determined by monitoring the emission decay curves within the $^5D_0 \rightarrow ^7F_2$ transition (613 nm) at room temperature and 10 K (see Figure S9, Supporting Information). The decay curves were well fitted by a single-exponential function, yielding lifetimes of 1.53 ± 0.02 and 1.62 ± 0.01 ms at room temperature with and without vacuum, respectively, and 2.02 ± 0.02 ms for the measurement at low temperature (10 K). These measurements are consistent with the presence of a single Eu^{3+} coordination environment and unequivocally demonstrate the effect of water release on the measured lifetime. Moreover, the residual effect of the vacuum on the lifetime clearly indicates that the water is not coordinated to the Eu^{3+} ions nor is it in their close vicinity, as previously described in the crystallographic section.

3.5. Thermal Behavior and Variable-Temperature Powder X-ray Diffraction. Thermal treatment of $[\text{Ln}(\text{H}_3\text{NMP})]\cdot 1.5\text{H}_2\text{O}$ compounds (**1**–**5**) under nitrogen atmosphere resulted in very similar decomposition processes which were ultimately reflected as identical thermograms (see Figure S10 in the Supporting Information). The thermal behavior for $[\text{Pr}(\text{H}_3\text{NMP})]\cdot 1.5\text{H}_2\text{O}$ (**2**) will be discussed in more detail in the following paragraph, with the conclusions also being valid for the remaining members of the series given the appropriate weight losses summarized in the Experimental Section.

$[\text{Pr}(\text{H}_3\text{NMP})]\cdot 1.5\text{H}_2\text{O}$ releases most of the interlayer water molecules of crystallization up to ca. 120 °C in two consecutive steps with DTG peaks at ca. 32 and 95 °C, respectively. The total observed weight loss is 5.3%, which is slightly

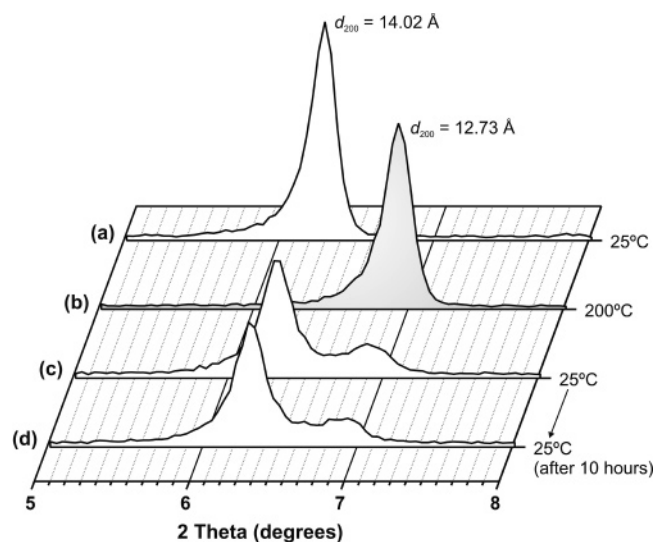


Figure 13. Evolution of the position of the first reflection of the PXRD patterns of $[\text{Pr}(\text{H}_3\text{NMP})]\cdot 1.5\text{H}_2\text{O}$ (**2**) during the in situ dehydration/rehydration study: (a) as-synthesized material collected at ambient temperature; (b) dehydrated material collected at 200 °C; (c) compound obtained immediately after slow cooling (inside the high-temperature chamber) of the dehydrated material, and (d) after 10 h. A profile of the temperature regime and the points where data were collected is provided in Figure S12 (Supporting Information).

lower than the expected value for the liberation of all water molecules (ca. 5.8%). Variable-temperature [powder X-ray diffraction studies (VTPXRD) for $[\text{Pr}(\text{H}_3\text{NMP})]\cdot 1.5\text{H}_2\text{O}$ (**2**) (see Figure S11 in the Supporting Information) show that the kinetics associated with release of water molecules between 25 and 125 °C is clearly distinct throughout this temperature range with the most significant loss being in the upper temperature region. Associated with this process, a new crystalline “dehydrated” phase is formed above 100 °C, having the first strong reflection right shifted with the corresponding d_{200} spacing of about 12.73 Å (Figure 13). Nevertheless, as notably evidenced in the VTPXRD study at 125 °C, this phase transformation is not complete, which unequivocally accounts for the discrepancy stated above in the amount of released water. The phase transformation is only complete at ca. 200 °C (see Figure S11) with the dehydrated material being thermally stable up to approximately 330 °C. In this interval TG analysis clearly shows a small weight loss, mainly below 200 °C, attributed to the release of residual water.

The new dehydrated crystalline phase clearly has a shorter a axis when compared with $[\text{Pr}(\text{H}_3\text{NMP})]\cdot 1.5\text{H}_2\text{O}$ (**2**), as evidenced in Figure 13. The powder pattern collected at 200 °C was indexed using DICVOL04²⁸ (17 reflections, fixed absolute error on each line of $0.03^\circ 2\theta$, no impurities allowed) with the calculated unit cell parameters being $a = 25.08$ Å, $b = 12.45$ Å, and $c = 7.91$ Å, having acceptable figures-of-merit [$M(17)^{29} = 5.0$ and $F(17)^{30} = 4.5$]. This X-ray diffraction evidence seems to indicate that by thermal heating the main structural features of the 2D layers do not change. Indeed, adjacent layers (as depicted in Figure 5a)

(28) Boulton, A.; Louer, D. *J. Appl. Crystallogr.* **2004**, *37*, 724–731.

(29) Boulton, A.; Louer, D. *J. Appl. Crystallogr.* **1991**, *24*, 987–993.

(30) Louer, D. In *Automatic Indexing: Procedures and Applications, Accuracy in Powder Diffraction II*; Gaithersburg, MD, 1992; pp 92–104.

(27) Fernandes, J. A.; Ferreira, R. A. S.; Pillinger, M.; Carlos, L. D.; Jepsen, J.; Hazell, A.; Ribeiro-Claro, P.; Gonçalves, I. S. *J. Lumin.* **2005**, *113*, 50–63. Auzel, F.; Malta, O. L. *J. Phys. (Paris)* **1983**, *44*, 201–206.

simply become mutually closer in an attempt to remove the void imposed by the release of the water molecules with the overall crystal symmetry remaining basically unaltered. This assumption is in agreement with the photoluminescence properties registered for $[\text{Eu}(\text{H}_3\text{NMP})]\cdot 1.5\text{H}_2\text{O}$ (**5**) under vacuum plus some preliminary ^{13}C solid-state NMR studies (data not shown) on dehydrated $[\text{La}(\text{H}_3\text{NMP})]\cdot 1.5\text{H}_2\text{O}$ (**1**), which displays the exact same resonances as the as-synthesized compound (Figure 6a). Once the temperature is decreased, the material readily re-absorbs water from the surrounding environment (Figure 13c). It is feasible to assume that this “sponge”-type behavior occurs naturally as an attempt to re-establish the strong hydrogen-bonding subnetwork described in the previous sections. Nevertheless, the process is not completely reversible and after the initial absorption of water the material remains unaltered with time (Figure 13d).

After ca. 330 °C the thermal decomposition of the organic component associated with the $\text{H}_3\text{NMP}^{3-}$ residues settles in, mainly involving two major weight losses, which are practically consecutive (Figure S10 in the Supporting Information). The obtained residues at 700 °C could not be identified from in-situ PXRD due to their poor crystallinity, but it is feasible to assume that they should correspond to a mixture of lanthanide phosphates with lanthanide oxides.^{9,31}

3.6. Vibrational Spectroscopy. The vibrational ATR-FTIR and FT Raman spectra of $[\text{Ln}(\text{H}_3\text{NMP})]\cdot 1.5\text{H}_2\text{O}$ are particularly informative, providing supporting evidence for the structural aspects previously described using synchrotron PXRD and solid-state NMR studies.³² Figure S13 in the Supporting Information shows selected regions of the spectra for the $[\text{Ln}(\text{H}_3\text{NMP})]\cdot 1.5\text{H}_2\text{O}$ series. As in previous sections, only the details for $[\text{Pr}(\text{H}_3\text{NMP})]\cdot 1.5\text{H}_2\text{O}$ (**2**) are discussed.

Amine protonation of the anionic ligand $\text{H}_3\text{NMP}^{3-}$ is particularly evident in the vibrational spectra with clearly visible diagnostic bands attributed to $\nu_s(\text{N}-\text{H})$ (involved in hydrogen bonds): a sharp (medium intensity) band observed at ca. 3110 cm^{-1} in the FTIR spectrum plus and a weak, mainly broad, band centered at ca. 3114 cm^{-1} in FT Raman. The presence of the diagnostic stretching bands (ν , symmetric and asymmetric) associated with the $-\text{CH}_2-$ groups is markedly visible in the spectra, giving rise to the sharp peaks around 3000 cm^{-1} . Still in this spectral region a broad band is clearly visible and attributed to the stretching vibrational modes of the $\text{PO}-\text{H}$ functional groups. Indeed, when compared with the analogous vibrational energies for free phosphonate groups (which typically appear around 2800 cm^{-1}), the vibrations in **2** are slightly shifted to lower wavenumbers (peaking around 2770 cm^{-1}), most likely due to their involvement in the hydrogen-bonding interactions previously described in the crystallographic section. A number of FTIR bands are also present in the 2320–2360 region, also attributed to the $\nu(\text{PO}-\text{H})$ stretching modes, thus confirming the presence of protonated phosphonate groups.^{13,31,33}

In the FTIR spectral region between 3600 and 2500 cm^{-1} a broad band (peaking at ca. 3356 cm^{-1}) is attributed to the $\nu(\text{O}-\text{H})$ of water molecules involved in the hydrogen bonds.

In the spectral range between 1200 and 900 cm^{-1} there are a number of intense and sharp peaks, either in FTIR and FT Raman, which arise from distinct stretching vibrational modes associated with the many different $\text{P}-\text{O}$ bonds present in the crystal structure of **2** and previously described in detail (see section dedicated to crystal description). While the bands at higher wavenumbers (1185 and 1164 cm^{-1} in the FTIR and 1162 cm^{-1} in FT Raman spectra) can be assigned to $\nu_s(\text{P}=\text{O})$, those in the lower wavenumber region (911 and 916 cm^{-1} in FTIR and FT Raman spectra, respectively) are instead attributed to the $\nu_s(\text{P}-\text{OH})$ vibrational mode. Finally, the FTIR band at 1066 cm^{-1} (1078 cm^{-1} in FT Raman) and the two bands at 1021 and 998 cm^{-1} (only one centered at ca. 1011 cm^{-1} in the FT Raman spectrum) are attributed to $\nu_{\text{as}}(\text{P}-\text{O}_{\text{coord}})$ and $\nu_s(\text{P}-\text{O}_{\text{coord}})$, respectively. The two latter vibrational bands are shifted to lower wavenumbers when compared to those of the uncoordinated ligand, thus indicating coordination to the lanthanide cations.^{13,33}

4. Conclusions

A new series of powdered 2D LnOFs, $[\text{Ln}(\text{H}_3\text{NMP})]\cdot 1.5\text{H}_2\text{O}$ [$\text{Ln}^{3+} = \text{La}^{3+}$ (**1**), Pr^{3+} (**2**), Nd^{3+} (**3**), Sm^{3+} (**4**), or Eu^{3+} (**5**) and $\text{H}_3\text{NMP}^{3-}$ is a residue of nitrilotris(methylene-phosphonic acid)], has been prepared using the hydrothermal method. The structure of these materials has been studied with a plethora of techniques, particularly high-resolution synchrotron PXRD collected on $[\text{Pr}(\text{H}_3\text{NMP})]\cdot 1.5\text{H}_2\text{O}$ and high-resolution solid-state NMR performed on $[\text{La}(\text{H}_3\text{NMP})]\cdot 1.5\text{H}_2\text{O}$. The present study clearly shows the power of this combined approach when suitable LnOF single crystals are not available. As shown by variable-temperature PXRD and photoluminescence spectroscopy, the $[\text{Ln}(\text{H}_3\text{NMP})]\cdot 1.5\text{H}_2\text{O}$ system is structurally robust, accepting removal of the water molecules of crystallization located within the interlayer spaces. Molecules other than water may perhaps be introduced (and removed) into these materials, tuning the photoluminescence properties. Moreover, we are at present investigating the structural modifications in the isolated networks (namely, the dimensionality and the topological aspects) induced by varying the number of phosphonic acid groups of the organic primary building block.

Supporting Information Available: Detailed experimental information on the powder X-ray diffraction, solid-state NMR, and photoluminescence studies; Le Bail whole powder diffraction pattern profile fittings for $[\text{Ln}(\text{H}_3\text{NMP})]\cdot 1.5\text{H}_2\text{O}$ (where $\text{Ln}^{3+} = \text{La}^{3+}$, Nd^{3+} , Sm^{3+} , and Eu^{3+}); $^5\text{D}_0$ decay curves recorded at room temperature and 10 K for $[\text{Eu}(\text{H}_3\text{NMP})]\cdot 1.5\text{H}_2\text{O}$; thermograms between ambient temperature and 700 °C for $[\text{Ln}(\text{H}_3\text{NMP})]\cdot 1.5\text{H}_2\text{O}$; VTPXRD patterns for $[\text{Eu}(\text{H}_3\text{NMP})]\cdot 1.5\text{H}_2\text{O}$ between ambient temperature and 300 °C (10 sampled temperatures); temperature

(31) Bestaoui, N.; Bakhmutova-Albert, E. V.; Rodriguez, A. V.; Llavona, R.; Clearfield, A. *Eur. J. Inorg. Chem.* **2005**, 829–836.

(32) Socrates, G. *Infrared Characteristic Group Frequencies-Tables and Charts*, 2nd ed.; John Wiley & Sons Ltd: Baffins Lane, Chichester, 1994.

(33) Martinez-Tapia, H. S.; Cabeza, A.; Bruque, S.; Pertierra, P.; Garcia-Granda, S.; Aranda, M. A. G. *J. Solid State Chem.* **2000**, 151, 122–129. Barja, B. C.; Herszage, J.; Alfonso, M. D. *Polyhedron* **2001**, 20, 1821–1830. Kong, D. Y.; Li, Y.; Xiang, O. Y.; Prosvirin, A. V.; Zhao, H. H.; Ross, J. H.; Dunbar, K. R.; Clearfield, A. *Chem. Mater.* **2004**, 16, 3020–3031.

program employed in the study of the reversible dehydration–rehydration of $[\text{Eu}(\text{H}_3\text{NMP})]\cdot 1.5\text{H}_2\text{O}$; selected spectral regions of the ATR-FTIR spectra for $[\text{Ln}(\text{H}_3\text{NMP})]\cdot 1.5\text{H}_2\text{O}$. This material is available free of charge via the Internet at <http://pubs.acs.org>.

Acknowledgment. We are grateful to Fundação para a Ciência e Tecnologia (FCT, Portugal) for their generous

financial support (POCI/QUI/58377/2004 supported by FEDER) and postdoctoral scholarship no. SFRH/BPD/14410/2003 (to L.C.-S.). We also wish to thank the ESRF (Grenoble, France) for access to the high-resolution powder diffractometer instrument assembled at the Swiss-Norwegian BM01b beam line.

CM070596Q